


Prevalence of oxygen defects in an in-plane anisotropic transition metal dichalcogenide

Ryan Plumadore ¹, Mehmet Baskurt ⁵, Justin Boddison-Chouinard,¹ Gregory Lopinski,² Mohsen Modarresi ³,
Pawel Potasz ⁴, Pawel Hawrylak,¹ Hasan Sahin ⁵, Francois M. Peeters ⁶ and Adina Luican-Mayer ^{1,*}

¹*Department of Physics, University of Ottawa, Ottawa, Canada*


²*National Research Council, Ottawa, Canada*

³*Department of Physics, Ferdowsi University of Mashhad, Mashhad, Iran*

⁴*Department of Theoretical Physics, Wroclaw University of Science and Technology, Wroclaw, Poland*

⁵*Department of Photonics, Izmir Institute of Technology, 35430 Urla, Izmir, Turkey*

⁶*Department of Physics, University of Antwerp, Groenenborgerlaan 171, B-2020 Antwerpen, Belgium*

 (Received 18 May 2020; revised 13 October 2020; accepted 15 October 2020; published 9 November 2020)

Atomic scale defects in semiconductors enable their technological applications and realization of different quantum states. Using scanning tunneling microscopy and spectroscopy complemented by *ab initio* calculations we determine the nature of defects in the anisotropic van der Waals layered semiconductor ReS₂. We demonstrate the in-plane anisotropy of the lattice by directly visualizing chains of rhenium atoms forming diamond-shaped clusters. Using scanning tunneling spectroscopy we measure the semiconducting gap in the density of states. We reveal the presence of lattice defects and by comparison of their topographic and spectroscopic signatures with *ab initio* calculations we determine their origin as oxygen atoms adsorbed at lattice point defect sites. These results provide an atomic-scale view into the semiconducting transition metal dichalcogenides, paving the way toward understanding and engineering their properties.

DOI: [10.1103/PhysRevB.102.205408](https://doi.org/10.1103/PhysRevB.102.205408)

Intrinsic defects, such as grain boundaries, vacancies, adatoms, and substitutional impurities are ubiquitously present in graphene and transition metal dichalcogenides (TMDs) [1–4]. Harnessing the properties of TMDs for atomic scale optoelectronic devices requires detailed understanding of the nature and effects of structural lattice defects on the material properties. Defects can influence the performance of devices through the formation of electronic states within the semiconducting gap [5,6], can modify the excitonic transitions and photoluminescence response [7], can behave as atomlike quantum emitters [8,9], and can affect the catalytic properties [10]. Although imaging techniques visualized surface defects of bulk TMDs [11–13], identifying their nature and correlating their presence with properties of the material remains challenging. For example, one of the most common imaging techniques, electron microscopy, can result in knock-on sputtering of chalcogen atoms [13], making it impossible to distinguish the intrinsic defects. Moreover, in the case of some TMDs like ReS₂, the larger atomic number of the metal can prevent identifying the nature of defects. Therefore, non-invasive techniques like scanning tunneling microscopy and spectroscopy (STM/STS) can be invaluable in imaging and determining the properties of lattice defects.

Here, we use a combination of STM/STS [Fig. 1(a)] in tandem with *ab initio* calculations to determine the structural and electronic properties of ReS₂ and its defects. These experimental and theoretical results indicate that a common defect

corresponds to oxygen atoms adsorbed at lattice point defect sites.

While most van der Waals (vdW) layered materials are isotropic within the plane, a number of them have lower in-plane crystal symmetry [14]. In-plane anisotropy in layered vdW materials gives additional functionality that has only just begun to be explored in black phosphorus (BP) [15], transition metal trichalcogenides (TiS₃) [16], rhenium disulfide (ReS₂), and rhenium diselenide (ReSe₂) [17]. Among them, ReS₂ attracted attention as a material that is stable under ambient conditions, with structural anisotropy that translates into further tunability in its electronic [18,19], optical [20–23], and mechanical [24] properties. Structurally, ReS₂ is a distorted 1T structure which belongs to the $P\bar{1}$ space group [25,26]. The additional electron in the *d* orbital of the rhenium atoms favors the existence of metallic Re-Re bonds, responsible for the formation of a superlattice of chains with diamond clusters of four Re atoms, as shown schematically in Fig. 1(b). This structure was previously visualized by x-ray spectroscopy [25,27] and electron microscopy [13]. Early scanning probe microscopies provided also indications of a Re chain structure [28–30]. When cleaved, the crystal orientation of the ReS₂ flakes is apparent, as they maintain the edges parallel to the rhenium chains. This feature is useful for identifying the orientation of a crystal for example in device fabrication [18,31]. Indeed, in the large area STM topographic images, as presented in Fig. 1(c), we find that terraces on the surface of ReS₂ follow the crystallographic directions with an angle $\gamma \approx 120^\circ$ between the *a* and *b* directions. The terraces and steps in Fig. 1(c) correspond to single or double atomic layers, with their height measured as shown in the inset.

*luican-mayer@uottawa.ca

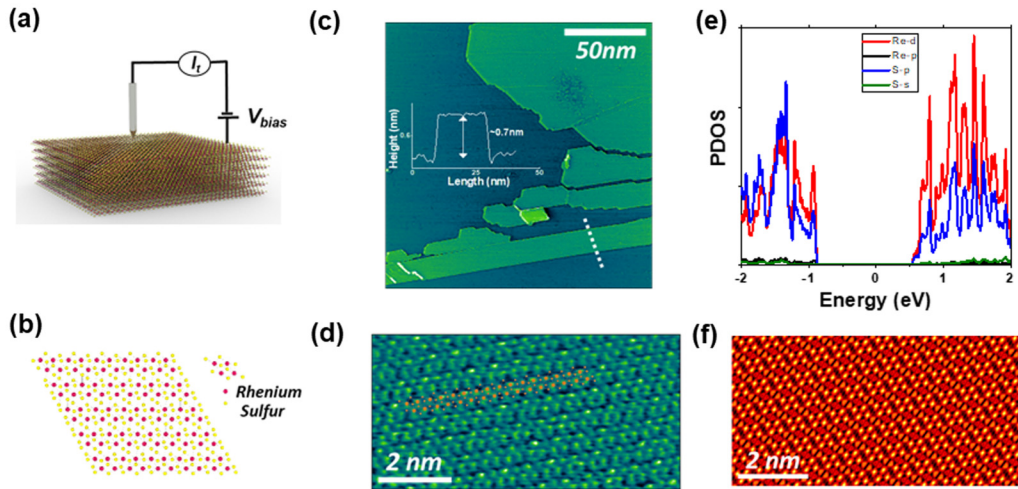


FIG. 1. (a) Schematic of the STM experiment. (b) Top and side view of the ReS_2 structure. (c) STM topographic map of step edges on the surface of a ReS_2 crystal ($V_b = -1.60$ V; $I_T = 450$ pA). Inset: Height profile along the white dotted line. (d) STM topographic image highlighting the Re chains with a spheres model as a guide to the eye. (e) Calculated PDOS of monolayer ReS_2 . (f) Simulated STM image of the ReS_2 lattice.

In higher resolution images, presented in Fig. 1(d), we observe the characteristic anisotropic lattice structure with elongated chains. One might be tempted to attribute the measured features to the topmost layer of sulfur (S) atoms [30] which is closest to the tip. However, a more accurate interpretation reveals that the contrast in the atomically resolved STM topographic images originates from local density of states (LDOS). Therefore, the complex dependence of the partial density of states (PDOS) at the surface layer on the energy at which the tunneling process occurs must be considered. The calculated PDOS using *ab initio* theory is shown in Fig. 1(e). The density of states is dominated by the rhenium- d orbitals, which is related to the flat band dispersion around the top of the valence band (VB) at the Γ point. At higher energies, band crossings lead to a substructure in the density of states. We find that within the energy range of our experiment the rhenium d orbitals [in red in Fig. 1(e)] are responsible for the largest contribution to the density of states. This implies that the metal atoms are predominantly involved in the tunneling process and therefore provide the contrast in the atomically resolved topographic images. This is further confirmed by simulated images (as detailed in the Methods section) of the STM measurement in Fig. 1(f).

We now turn our attention to the band structure of ReS_2 . Electronically, ReS_2 is a semiconductor, however, the nature of the semiconducting gap (direct or indirect) in the bulk versus monolayers remains a subject of discussion both experimentally and theoretically [13,32–39]. A number of experimental techniques including optical spectroscopies and electronic transport found the bulk band gap to be in the range of 1.40 ± 0.07 eV [13,15,17,18,40], in agreement with results of theoretical calculations which reported the band gap to be in the range of 1.4 ± 0.1 eV [13,14,16,19,20,34–39]. However, transport and optical spectroscopy are macroscopic measurements which average over large areas of a crystal. Here, we use a local probe, scanning tunneling microscopy, and spectroscopy to measure the density of states on the surface of ReS_2 crystals. We find that the differential con-

ductance, in Fig. 2(a), shows the presence of an energy gap confirming the semiconducting nature of ReS_2 . The extracted value of the energy gap is 1.35 ± 0.1 eV, agreeing with previous experiments. We note that this spectrum, Fig. 2(a), represents averages over different samples, areas, and tips as detailed in the Supplemental Material [41], and it is plotted on a logarithmic scale [42] for clarity. In Fig. 2(b) we show

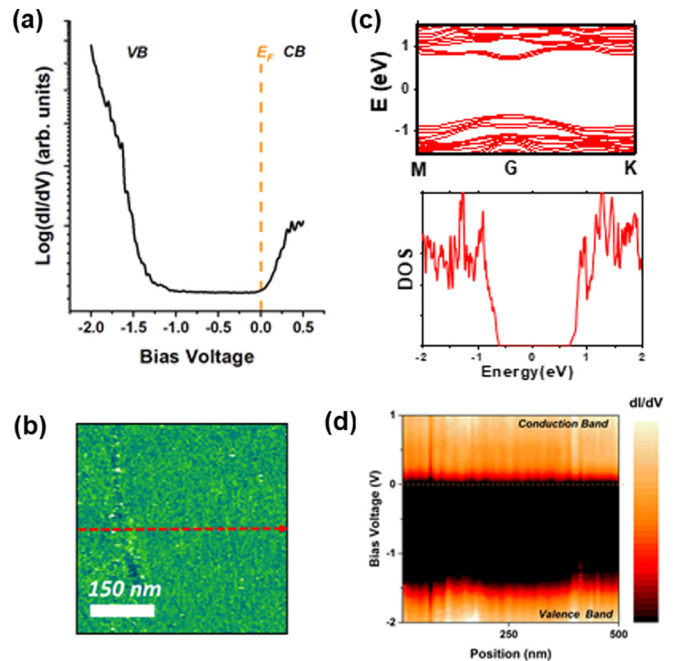


FIG. 2. (a) Scanning tunneling spectroscopy averaged on the surface of ReS_2 . The logarithmic scale was used to highlight valence band (VB) and conduction band (CB) whose band edges relative to the Fermi level (E_F) are also indicated by arrows. (b) Right: line map of the scanning tunneling spectrum across the dashed line indicated in the topographic image in the left ($V_b = -1.00$ V; $I_T = 65$ pA). (c) Band structure of three-layer ReS_2 and the corresponding DOS. (d) Color map of the differential conductance dI/dV vs Bias Voltage (V) and Position (nm), showing the conduction band and valence band regions.

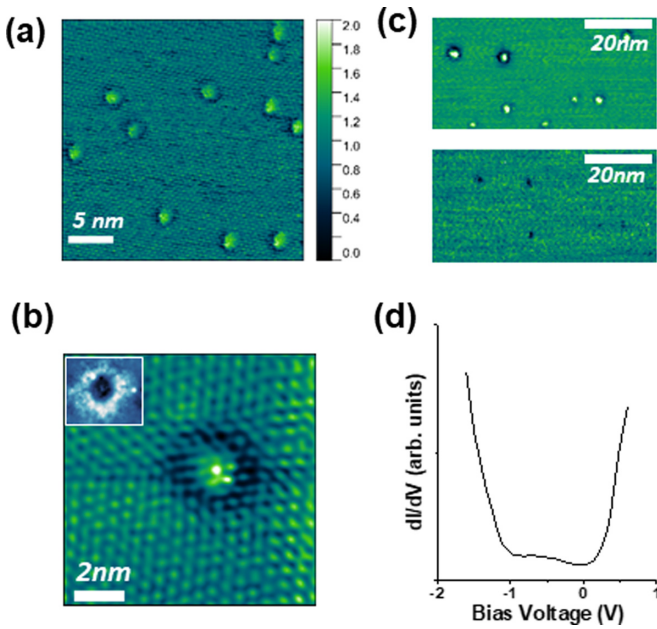


FIG. 3. (a) STM topographic image ($V_b = -1.20$ V; $I_T = 80$ pA) showing lattice defects. (b) Topographic high-resolution image across a defect. Inset: LDOS map across a defect at $V_b = -1.2$ V and $I_T = 35$ pA. (c) STM topographic images ($I_T = 50$ pA) of an area at different bias voltages. Top: $V_{\text{bias}} = -0.80$ V; bottom: $V_{\text{bias}} = +0.80$ V. (d) Averaged STS measured on 22 defects such as the one in (b).

the spatial variation of the spectrum across the device-size area, topographically presented in the left panel by plotting the scanning tunneling spectra across the dashed line (right panel). Within our resolution, the variation of the energy gap is less than 0.1 eV. These experimental findings are now compared with our theoretical calculations. In Fig. 2(c) we show the band structure and corresponding DOS of a slab of ReS_2 consisting of three layers with details of calculations in the Supplemental Material [41]. The calculations show a gap at

the Γ point, and from the corresponding DOS we can estimate the energy gap around $E_{\text{gap}} = 1.3$ eV, in good agreement with the measured semiconducting energy gap. While the density-functional theory (DFT) gap appears to be in good agreement with the measured semiconducting energy gap, we note that DFT underestimates the energy gap. Inclusion of many-body corrections at the GW_0 quasiparticle level increases the band gap to 2.3 eV. However, we note that the blueshift of quasiparticle transition energies is partially compensated by excitonic effects which reduces the optical gaps to values often consistent with DFT band gaps. In a STS measurement, the zero bias corresponds to the Fermi level (E_F) as indicated by the dashed line in Fig. 2(a). In an electrically neutral ReS_2 , we expect the position of E_F to be in the middle of the semiconducting gap. However, in our samples we find the position of E_F to be close to the bottom of the conduction band (E_C), indicating the crystal is n doped.

We now turn to the analysis of dopants and defects. When imaging the surface of the ReS_2 crystal, we encounter “bright” or “dark” regions representing the presence of a dopant or defect that will electrostatically interact with its environment. Such features have been previously reported on surfaces of doped III–V semiconductors [43], topological insulators [44], transition metal dichalcogenides [45,46], BP [47,48], or BN [49] Fig. 3(b). The most common type of defects are shown in the STM topographic image of Fig. 3(a). They have a characteristic bright center with a dark halo when imaged at negative bias voltages [Fig. 3(b)]. As we vary the scanning parameters, we observe that the apparent height of the defects changes, so that they appear bright at negative bias voltages and dark at positive bias voltages. This is demonstrated in Fig. 3(c) where we present STM topographic images taken at different bias voltages: -0.80 and $+0.80$ V respectively. The spectroscopic data acquired on the center of the defects, and presented in Fig. 3(d) as an average over 22 defects and in the Supplemental Material [41] on only one defect, closely resemble the one on a defect-free area, and reveal the absence of in-gap states. The slight increase in DOS within the gap in Fig. 3(d) could be due to buried defects under the

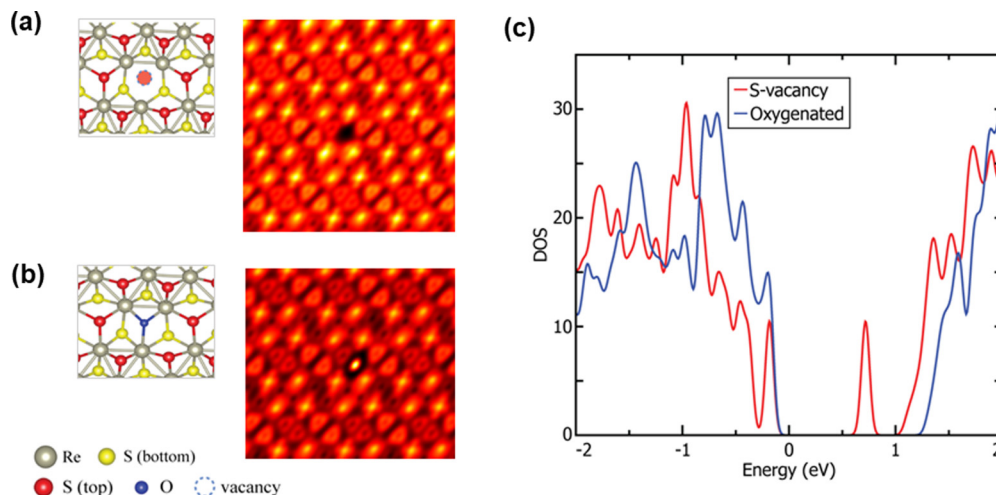


FIG. 4. Crystal structure and simulated STM images of (a) S vacancy and (b) O absorbed by S vacancy. (c) LDOS of S vacancy and O absorbed by S vacancy.

surface, as previously seen in other TMDs [50]. To complement our STM/STS data, we performed X-ray Photoelectron Spectroscopy (XPS) analysis of the crystal and, in addition to the expected Re and S [51,52], we also find the presence of oxygen as shown in the Supplemental Material [41].

Different possible atomic scale defects in the lattice of ReS₂ can have signatures in an STM experiment. For example, defects, such as a single atom vacancy, single atom adsorption, antisite formation where the S atom is substituted by the Re atom or vice versa, can be formed during the growth of two-dimensional (2D) ReS₂ sheets. To elucidate the possible origins of the most common defects observed in our STM experiments on the surface of ReS₂ we used DFT calculations. Simulated STM images of pristine ReS₂ and defected structures, together with their characteristic density of states, are presented in Fig. 4. The formation of such defects results in dangling bonds within the lattice, which are readily oxygenated under atmospheric conditions, leading to O atom absorption by vacancies within the lattice. In fact, our theoretical results show that oxygen absorption by an S vacancy, as presented in Fig. 4(b), will create signatures in the density-of-states maps that closely resemble the measured defects, with a distinctive halo structure. Moreover, when we examine the density of states, a S vacancy results in midgap states [red curve in Fig. 4(c)], while when an O atom is bound to the S vacancy, the semiconducting band gap changes only slightly, in agreement with our experimental finding from STS presented in Fig. 3(e), strengthening the case for oxygen being a common defect in the ReS₂ layers. These results are also consistent with the reports that oxygen is a source of atomic-scale defects in MoS₂ [11,12].

We note that in addition to the defects discussed in Fig. 3, we also observed less frequent types of lattice defects as discussed in the Supplemental Material [41].

In summary, we presented results of scanning tunneling microscopy and spectroscopy together with *ab initio* DFT calculations of the nanoscale lattice structure, electronic band gap, and defects of in-plane anisotropic semiconducting ReS₂. We resolve the chains of rhenium atoms forming diamond-shaped clusters, we measure the semiconducting energy gap and compare the experimental values with results of *ab initio* calculations. Moreover, we reveal the presence of atomic lattice defects and explore their local properties. By comparing their signatures in the STM/STS experiment with the theoretical calculations, we identify that oxygen is frequently absorbed at defect sites in this material. As the nature of atomic defects is critical in understanding the properties of 2D materials, our result paves the way toward understanding and engineering properties of in-plane anisotropic 2D semiconductors.

METHODS

Theory. The calculations of energy bands, the band gap, and density of states in a single layer and a slab consisting of three layers of ReS₂ were done using the Quantum ESPRESSO code, with cutoff energy 70 Ry and mesh of $25 \times 25 \times 1 k$ grid. Each layer/slab was separated by 20 Å of vacuum and

the structure was fully relaxed. Vienna *ab initio* Simulation Package (VASP) and plane-wave projector-augmented wave (PAW) potentials were used in the calculations [47]. The generalized gradient approximation (GGA) form of Perdew-Burke-Ernzerhof (PBE) was used for the exchange-correlation functional [48]. The kinetic energy cutoff of the plane-wave basis set was taken to be 400 eV. For the structural optimization and LDOS calculations a Gaussian broadening width of 0.05 eV was taken. The convergence criterion between consequent electronic steps was set at 10^{-5} eV. Gamma centered k mesh was taken as $5 \times 5 \times 1$ and $10 \times 10 \times 1$ for structural optimization and LDOS calculations, respectively, for $2 \times 2 \times 1$ supercell. At least 15 Å of vacuum spacing between layers was taken in order to prevent any interactions between layers. STM images were simulated by calculating partial charge densities in the range $[-2, 0]$ and $[-2, 2]$ eV of the cells, and using the formula

$$E_{\text{total}} = \sum_n^h E_n e^{-kz_n},$$

where E_{total} is the summed charge density matrix, n is the layer number, h is the height of the ReS₂ monolayer, E_n is the n th layer partial charge density matrix, k is a constant, and z_n is the distance from the artificial STM tip in the z direction. Contrast changes as a result of the bias voltage were simulated by involving electron doped conduction bands in a range of 2 eV.

STM/STS. We use a commercial RHK Pan Freedom system with ultrahigh vacuum (UHV) and variable temperature capabilities. The data here are taken at temperatures 80–300 K.

Sample preparation. In this study we use commercial (HQ graphene) bulk crystals ReS₂ cleaved in air and subsequently introduced into ultrahigh vacuum (UHV).

XPS. The XPS spectra were measured on a Kratos Axis Nova spectrometer equipped with an Al x-ray source. The XPS data were collected using Al- $K\alpha$ radiation at 1486.69 eV (150 W, 10 mA), charge neutralizer and a delay-line detector (DLD) consisting of three multichannel plates.

ACKNOWLEDGMENTS

The authors acknowledge funding from National Sciences and Engineering Research Council (NSERC) Discovery Grant No. RGPIN-2016-06717. We also acknowledge the support of the Natural Sciences and Engineering Research Council of Canada (NSERC) through QC2DM Strategic Project No. STPGP 521420. P.H. thanks uOttawa Research Chair in Quantum Theory of Materials for support. P.P. acknowledges partial financial support from National Science Center (NCN), Poland, Grant Maestro No. 2014/14/A/ST3/00654, and calculations were performed in the Wrocław Center for Networking and Supercomputing. H.S. acknowledges financial support from TUBITAK under Project No. 117F095 and from Turkish Academy of Sciences under the GEBIP program. Our computational resources were provided by TUBITAK ULAKBIM, High Performance and Grid Computing Center (TR-Grid e-Infrastructure).

- [1] S. Manzeli, D. Ovchinnikov, D. Pasquier, O. V. Yazyev, and A. Kis, *Nat. Rev. Mater.* **2**, 17033 (2017).
- [2] Z. Lin, B. R. Carvalho, E. Kahn, R. Lv, R. Rao, H. Terrones, M. A. Pimenta, and M. Terrones, *2D Mater.* **3**, 022002 (2016).
- [3] A. Luican-Mayer, J. E. Barrios-Vargas, J. T. Falkenberg, G. Autès, A. W. Cummings, D. Soriano, G. Li, M. Brandbyge, O. V. Yazyev, S. Roche, and E. Y. Andrei, *2D Mater.* **3**, 031005 (2016).
- [4] A. Luican-Mayer, G. Li, and E. Y. Andrei, *J. Electron Spectrosc. Relat. Phenom.* **219**, 92 (2017).
- [5] H. Qiu, T. Xu, Z. Wang, W. Ren, H. Nan, Z. Ni, Q. Chen, S. Yuan, F. Miao, F. Song, G. Long, Y. Shi, L. Sun, J. Wang, and X. Wang, *Nat. Commun.* **4**, 2642 (2013).
- [6] J. Shim, S. Oh, D.-H. Kang, S.-H. Jo, M. H. Ali, W.-Y. Choi, K. Heo, J. Jeon, S. Lee, M. Kim, Y. J. Song, and J.-H. Park, *Nat. Commun.* **7**, 13413 (2016).
- [7] S. Tongay, J. Suh, C. Ataca, W. Fan, A. Luce, J. S. Kang, J. Liu, C. Ko, R. Raghunathanan, J. Zhou, F. Ogletree, J. Li, J. C. Grossman, and J. Wu, *Sci. Rep.* **3**, 2657 (2013).
- [8] M. Atatüre, D. Englund, N. Vamivakas, S.-Y. Lee, and J. Wrachtrup, *Nat. Rev. Mater.* **3**, 38 (2018).
- [9] G. Grosso, H. Moon, B. Lienhard, S. Ali, D. K. Efetov, M. M. Furchi, P. Jarillo-Herrero, M. J. Ford, I. Aharonovich, and D. Englund, *Nat. Commun.* **8**, 705 (2017).
- [10] Y. Zhou, E. Song, J. Zhou, J. Lin, R. Ma, Y. Wang, W. Qiu, R. Shen, K. Suenaga, Q. Liu, J. Wang, Z. Liu, and J. Liu, *ACS Nano* **12**, 4486 (2018).
- [11] S. Barja, S. Refaely-Abramson, B. Schuler, D. Y. Qiu, A. Pulkín, S. Wickenburg, H. Ryu, M. M. Ugeda, C. Kastl, C. Chen, C. Hwang, A. Schwartzberg, S. Aloni, S.-K. Mo, D. Frank Ogletree, M. F. Crommie, O. V. Yazyev, S. G. Louie, J. B. Neaton, and A. Weber-Bargioni, *Nat. Commun.* **10**, 3382 (2019).
- [12] B. Schuler, D. Y. Qiu, S. Refaely-Abramson, C. Kastl, C. T. Chen, S. Barja, R. J. Koch, D. F. Ogletree, S. Aloni, A. M. Schwartzberg, J. B. Neaton, S. G. Louie, and A. Weber-Bargioni, *Phys. Rev. Lett.* **123**, 076801 (2019).
- [13] Y.-C. Lin, H.-P. Komsa, C.-H. Yeh, T. Björkman, Z.-Y. Liang, C.-H. Ho, Y.-S. Huang, P.-W. Chiu, A. V. Krasheninnikov, and K. Suenaga, *ACS Nano* **9**, 11249 (2015).
- [14] J. A. Wilson and A. D. Yoffe, *Adv. Phys.* **18**, 193 (1969).
- [15] X. Ling, H. Wang, S. Huang, F. Xia, and M. S. Dresselhaus, *Proc. Natl. Acad. Sci. USA* **112**, 4523 (2015).
- [16] J. Dai and X. C. Zeng, *Angew. Chem. Int. Ed.* **54**, 7572 (2015).
- [17] M. Rahman, K. Davey, and S.-Z. Qiao, *Adv. Funct. Mater.* **27**, 1606129 (2017).
- [18] E. Liu, Y. Fu, Y. Wang, Y. Feng, H. Liu, X. Wan, W. Zhou, B. Wang, L. Shao, C.-H. Ho, Y.-S. Huang, Z. Cao, L. Wang, A. Li, J. Zeng, F. Song, X. Wang, Y. Shi, H. Yuan, H. Y. Hwang, Y. Cui, F. Miao, and D. Xing, *Nat. Commun.* **6**, 6991 (2015).
- [19] D. Ovchinnikov, F. Gargiulo, A. Allain, D. J. Pasquier, D. Dumcenco, C.-H. Ho, O. V. Yazyev, and A. Kis, *Nat. Commun.* **7**, 12391 (2016).
- [20] D. A. Chenet, O. B. Aslan, P. Y. Huang, C. Fan, A. M. van der Zande, T. F. Heinz, and J. C. Hone, *Nano Lett.* **15**, 5667 (2015).
- [21] O. B. Aslan, D. A. Chenet, A. M. van der Zande, J. C. Hone, and T. F. Heinz, *ACS Photonics* **3**, 96 (2016).
- [22] C. H. Ho, Y. S. Huang, K. K. Tiong, and P. C. Liao, *Phys. Rev. B* **58**, 16130 (1998).
- [23] S. Sim, D. Lee, A. V. Trifonov, T. Kim, S. Cha, J. H. Sung, S. Cho, W. Shim, M.-H. Jo, and H. Choi, *Nat. Commun.* **9**, 351 (2018).
- [24] S. Yu, H. Zhu, K. Eshun, C. Shi, M. Zeng, and Q. Li, *Appl. Phys. Lett.* **108**, 191901 (2016).
- [25] H. J. Lamfers, A. Meetsma, G. A. Wiegers, and J. L. de Boer, *J. Alloys Compd.* **241**, 34 (1996).
- [26] H. H. Murray, S. P. Kelty, R. R. Chianelli, and C. S. Day, *Inorg. Chem.* **33**, 4418 (1994).
- [27] B. Jariwala, D. Voiry, A. Jindal, B. A. Chalke, R. Bapat, A. Thamizhavel, M. Chhowalla, M. Deshmukh, and A. Bhattacharya, *Chem. Mater.* **28**, 3352 (2016).
- [28] S. P. Kelty, A. F. Ruppert, R. R. Chianelli, J. Ren, and M. H. Whangbo, *J. Am. Chem. Soc.* **116**, 7857 (1994).
- [29] K. Friemelt, S. Akari, M. C. Lux-Steiner, T. Schill, E. Bucher, and K. Dransfeld, *Ann. Phys. (Berlin, Ger.)* **504**, 248 (1992).
- [30] S. J. Jung, T. Jeong, J. Shim, S. Park, J.-H. Park, B. G. Shin, and Y. J. Song, *Curr. Appl. Phys.* **19**, 224 (2019).
- [31] F. Liu, S. Zheng, X. He, A. Chaturvedi, J. He, W. L. Chow, T. R. Mion, X. Wang, J. Zhou, Q. Fu, H. J. Fan, B. K. Tay, L. Song, R.-H. He, C. Kloc, P. M. Ajayan, and Z. Liu, *Adv. Funct. Mater.* **26**, 1169 (2016).
- [32] J. L. Webb, L. S. Hart, D. Wolverson, C. Chen, J. Avila, and M. C. Asensio, *Phys. Rev. B* **96**, 115205 (2017).
- [33] H.-X. Zhong, S. Gao, J.-J. Shi, and L. Yang, *Phys. Rev. B* **92**, 115438 (2015).
- [34] G.-L. Ignacio, R. Bojja Aditya, U. Nicolas, and F. M. Alberto, *2D Mater.* **3**, 045016 (2016).
- [35] M. Gehlmann, I. Aguilera, G. Bihlmayer, S. Nemšák, P. Nagler, P. Gospodarič, G. Zamborlini, M. Eschbach, V. Feyer, F. Kronast, E. Młyńczak, T. Korn, L. Plucinski, C. Schüller, S. Blügel, and C. M. Schneider, *Nano Lett.* **17**, 5187 (2017).
- [36] K. Dileep, R. Sahu, S. Sarkar, S. C. Peter, and R. Datta, *J. Appl. Phys.* **119**, 114309 (2016).
- [37] C. H. Ho, P. C. Liao, Y. S. Huang, T. R. Yang, and K. K. Tiong, *J. Appl. Phys.* **81**, 6380 (1997).
- [38] D. Cakir, H. Sahin, and F. M. Peeters, *Phys. Chem. Chem. Phys.* **16**, 16771 (2014).
- [39] Z. G. Yu, Y. Cai, and Y.-W. Zhang, *Sci. Rep.* **5**, 13783 (2015).
- [40] J. V. Marzik, R. Kershaw, K. Dwight, and A. Wold, *J. Solid State Chem.* **51**, 170 (1984).
- [41] See Supplemental Material at <http://link.aps.org/supplemental/10.1103/PhysRevB.102.205408> for more details about band-gap measurements on different samples, different types of defects, and XPS data of the samples.
- [42] M. M. Ugeda, A. J. Bradley, S.-F. Shi, F. H. da Jornada, Y. Zhang, D. Y. Qiu, W. Ruan, S.-K. Mo, Z. Hussain, Z.-X. Shen, F. Wang, S. G. Louie, and M. F. Crommie, *Nat. Mater.* **13**, 1091 (2014).
- [43] R. M. Feenstra, *Phys. Rev. B* **50**, 4561 (1994).
- [44] Y. S. Hor, A. Richardella, P. Roushan, Y. Xia, J. G. Checkelsky, A. Yazdani, M. Z. Hasan, N. P. Ong, and R. J. Cava, *Phys. Rev. B* **79**, 195208 (2009).
- [45] C.-P. Lu, G. Li, J. Mao, L.-M. Wang, and E. Y. Andrei, *Nano Lett.* **14**, 4628 (2014).
- [46] R. Plumadore, M. M. A. Ezzi, S. Adam, and A. Luican-Mayer, *J. Appl. Phys.* **128**, 044303 (2020).
- [47] B. Kiraly, N. Hauptmann, A. N. Rudenko, M. I. Katsnelson, and A. A. Khajetoorians, *Nano Lett.* **17**, 3607 (2017).

- [48] Z. Qiu, H. Fang, A. Carvalho, A. S. Rodin, Y. Liu, S. J. R. Tan, M. Telychko, P. Lv, J. Su, Y. Wang, A. H. Castro Neto, and J. Lu, *Nano Lett.* **17**, 6935 (2017).
- [49] D. Wong, J. Velasco, Jr., L. Ju, J. Lee, S. Kahn, H.-Z. Tsai, C. Germany, T. Taniguchi, K. Watanabe, A. Zettl, F. Wang, and M. F. Crommie, *Nat. Nanotechnol.* **10**, 949 (2015).
- [50] R. Addou, L. Colombo, and R. M. Wallace, *ACS Appl. Mater. Interfaces* **7**, 11921 (2015).
- [51] A. Khosravi, R. Addou, M. Catalano, J. Kim, and R. M. Wallace, *Materials* **12**, 1056 (2019).
- [52] T. Fujita, Y. Ito, Y. Tan, H. Yamaguchi, D. Hojo, A. Hirata, D. Voiry, M. Chhowalla, and M. Chen, *Nanoscale* **6**, 12458 (2014).